Soft Matter

PAPER

View Article Online
View Journal | View Issue

Cite this: *Soft Matter*, 2024, **20**, 4567

Heterogeneity-induced retraction in viscoelastic fluids following cessation of flow†

Patrick J. McCauley, ‡ Satish Kumar * and Michelle A. Calabrese *

Complex fluids including colloidal suspensions, microgels, and entangled wormlike micelles (WLMs) can develop heterogeneous flow regions under imposed steady shear. In some of these systems, the evolution to this flow state from rest is accompanied by flow reversal – when a portion of the fluid moves opposite to the imposed flow direction. Flow reversal was proposed to occur in shear startup when (1) the fluid has significant elasticity, and (2) the flow becomes heterogeneous immediately following the stress overshoot [McCauley *et al.*, *J. Rheol.*, 2023, **67**, 661–681]. To verify this hypothesis, a new method is developed for measuring flow heterogeneity. Upon cessation of the imposed flow, elasticity and flow heterogeneity cause retraction of the fluid, which is quantified with particle tracking velocimetry. Flow is stopped at key times during shear startup in two systems: a gel-like WLM that exhibits flow reversal before heterogeneous flow and a viscoelastic, fluid-like WLM that does not. The degree of flow heterogeneity is inferred from the shape and magnitude of velocity profiles measured during retraction. Flow heterogeneity develops earlier in gel-like WLMs – supporting the proposed flow reversal criteria. For comparison, heterogeneous Couette flows described with the upper-convected Maxwell or Germann–Cook–Beris models are analyzed. These theoretical flow problems confirm that stark differences in rheological properties across the flow geometry can cause significant fluid retraction and reproduce key features of the experimentally observed retraction. This new method can be used to extract quantitative information about spatially heterogeneous flows in viscoelastic complex fluids, whether or not flow reversal occurs.

Received 11th February 2024,
Accepted 21st May 2024

DOI: 10.1039/d4sm00203b

rsc.li/soft-matter-journal

1 Introduction

Heterogeneous shear flows, where the microstructure and rheological properties of a flowing material vary spatially within the flow geometry, occur frequently in complex fluids ranging from colloidal suspensions to microgels and surfactants.[1–3] In shear flows of entangled wormlike micelles (WLMs), substantial flow heterogeneity results in the formation of shear bands, regions of fluid with distinct shear rates, microstructures, and viscosities. Significant effort has been expended over the last few decades to understand how shear bands form in WLMs.[4–7] To address this question, many studies have examined the evolution of shear-banded flow from an initially homogeneous solution at rest.[8–12] In a frequently studied type of WLM, cetylpyridinium chloride surfactants with sodium salicylate (CPyCl-NaSal), shear bands are proposed to form by a "disentangle–re-entangle" mechanism[10,11] in shear startup, a flow protocol where a constant shear rate is suddenly imposed on a solution at rest. Here, WLMs are hypothesized to be homogeneously entangled at rest, to homogeneously disentangle in the region of maximum stress, and then to partially re-entangle at long times following the onset of shear banding.

McCauley *et al.* recently proposed a unique shear band formation mechanism in WLM gels – WLMs with very slow dynamics and an apparent yield stress[13] – formed from triblock polymers known as poloxamers.[14] Heterogeneous flows in these 15% wt poloxamer WLMs were likely due to a mechanism similar to that observed in some yield stress fluids.[15,16] Here, elastic stresses accumulate near the beginning of startup flow, which eventually exceed the apparent static yield stress of the WLM gel. At this point, the WLM gel begins to fluidize. As the shear stress is not uniform in concentric cylinder flow geometries, only a portion of the WLM gel that is closer to the inner cylinder (where the shear stress is greater) fluidizes. In some yield stress fluids, this fluidized region expands over time and the flow heterogeneity eventually disappears.[17] However, for these WLM gels, viscoelastic aging in the unyielded fluid region increases resistance to flow over time and prevents further fluidization, trapping the flow heterogeneity and creating distinct shear bands that persist indefinitely; this viscoelastic

Department of Chemical Engineering and Materials Science, University of Minnesota Twin Cities, Minneapolis, Minnesota 55455, USA.
E-mail: kumar030@umn.edu, mcalab@umn.edu; Tel: +1 612 625 2558, +1 612 625 2551

† Electronic supplementary information (ESI) available. See DOI: https://doi.org/10.1039/d4sm00203b

‡ Current affiliation: Department of Chemical and Biomolecular Engineering, University of Delaware, Newark, Delaware 19716, USA.

aging was shown to be related to an increase in the micelle entanglement density due to micelle elongation.[14] These coexisting fluidized and unyielded regions were proposed to have very different rheological properties – relaxation times, viscosities, and elastic moduli – as inferred by the exceptionally large difference in shear rate in each region.

The most significant piece of evidence that suggested a unique shear band formation mechanism in these WLM gels was a period of flow reversal – when a portion of the fluid moves opposite to the direction of the moving boundary – during shear startup.[12,14,18] Flow reversal preceding shear banding has been predicted in constitutive models of entangled polymer solutions and WLM fluids,[19–23] and this phenomenon is expected to be more intense in geometries with greater underlying inhomogeneity (*e.g.* concentric cylinders with larger ratio of outer to inner radii).[19,24] Despite these modeling predictions, flow reversal has not been observed experimentally in WLMs which form shear bands by the canonical disentangle–re-entangle mechanism.[10,11,25] However beyond WLM gels,[12,14,18,26] flow reversal has also been observed in complex fluids ranging from soft glassy materials to polymer solutions and microgels.[27–30] Based on the commonality of this behavior across soft materials, McCauley *et al.* postulated two requirements for flow reversal:[14] (1) the fluid must have substantial elasticity and (2) the flow must be heterogeneous when the shear stress decreases with time, immediately following the maximum stress "overshoot" in shear startup. In the 15% wt poloxamer WLM gels, flow reversal coincided with the rapid stress drop after the stress maximum. In the shear banding mechanism proposed for these WLM gels, the flow is heterogeneous during this time period because of the partial fluidization. However, in the disentangle–re-entangle mechanism, WLMs are homogeneously disentangled during the rapid drop in stress, and thus one criterion for flow reversal is not satisfied.

Validating the proposed heterogeneity criterion is difficult as measuring the evolution of the flow heterogeneity is challenging. Simultaneous rheology and particle tracking velocimetry (rheo-PTV), which is the primary technique used previously to quantify flow reversal,[12,14,18] has the required spatiotemporal resolution, and qualitatively identifying heterogeneous flow regions from the velocity profile is fairly straightforward once the flow stabilizes. However, measuring flow heterogeneity is nontrivial during the transient period between initially homogeneous flow and shear-banded flow. For example, during flow reversal in poloxamer WLM gels, the velocity profile becomes highly nonlinear, and the location of distinct heterogeneous flow regions – if formed – cannot be clearly identified. Additionally, the underlying forward flow counteracts flow reversal, meaning this phenomenon can be suppressed at higher shear rates,[14,26] which complicates correlations between flow reversal and flow heterogeneity.

To characterize flow heterogeneity, a classic rheology protocol, cessation of flow, is revisited here and investigated with rheo-PTV. In cessation of flow, shear startup is maintained for some time, t_c, after which the strain is held constant and the fluid is allowed to relax. Previously, these protocols have been used to measure WLM microstructure recovery after shear startup, *via* flow-small angle neutron scattering (SANS) and flow-small angle light scattering (SALS).[10,11] Rheo-PTV during flow cessation is not useful for purely viscous fluids, as the velocity must be zero across the flow geometry. However, fluids with elasticity can retract once the driving forces producing the flow are removed.[31] Rheo-PTV measurements revealed regions of retracting fluid after step-strain in entangled polymer solutions[32]; later modeling efforts suggested this behavior could arise due to an underlying elastic consecutive instability, where small heterogeneities grow into shear flows.[33]

Here, the connection between flow heterogeneity and fluid retraction upon cessation of flow following shear startup is explored in wormlike micelles. This work shows that if elastic fluids, like the WLMs investigated here, have significant spatial heterogeneity in the stress dissipation rate, substantial fluid retraction accompanies stress relaxation during cessation of flow. Here, fluid retraction refers to the fluid moving in the direction opposite of the imposed shear flow after the imposed flow has been stopped, whereas flow reversal refers to a portion of the fluid moving opposite to the direction of the moving boundary during imposed shear flow. This large degree of fluid retraction can be subsequently related to flow heterogeneity.

In this article, fluid retraction upon flow cessation is examined comprehensively in two model aqueous poloxamer WLMs with spatially heterogeneous rheological properties, using experimental, theoretical, and computational methods. Both WLM solutions contain the same poloxamer, P234, but have been previously shown to exhibit drastically different rheological properties.[14,34] Here, 4% wt P234 with 0.9 M sodium fluoride (NaF) forms a canonical, fast-breaking viscoelastic WLM solution,[34] which is expected to exhibit shear banding *via* the "disentangle–re-entangle" mechanism. Conversely, 15% wt P234 with 2 M sodium chloride (NaCl) forms a WLM gel[14] which is proposed to exhibit shear banding similar to that in aging yield stress fluids.

Flow heterogeneity during shear startup is characterized *via* cessation of flow experiments with rheo-PTV, where partial fluidization and fluid retraction are measured directly. These experiments are subsequently analyzed using refined rheo-PTV analysis methods; the simple, predictable trajectories of particles in the rheo-PTV flow geometry are exploited to accurately measure the velocity of particles that move very slowly. The experimental conclusions are then strongly supported by results from two theoretical flow problems: (1) Couette flow between parallel plates, and (2) Couette flow between concentric cylinders. In the first, the fluid constitutive behavior is modeled by two upper-convected Maxwell model fluids (two-UCM) with different rheological properties occupying adjacent but spatially distinct regions – a simplified representation of shear banded flow that can be solved analytically. In the second, the fluid behavior is modeled using the Germann–Cook–Beris (GCB) model,[20,21] which captures key flow phenomena in poloxamer WLM gels including flow reversal and the onset of flow heterogeneity immediately following the stress overshoot in startup flows.

The different magnitudes of fluid retraction measured *via* rheo-PTV following cessation of flow strongly support the

distinct shear band formation mechanisms proposed for each WLM system. The analytical solution to the first flow problem then reveals key quantitative relationships between heterogeneous fluid properties and fluid retraction. Finally, GCB model simulations are shown to capture key flow features from experiments. Importantly, the degree of fluid heterogeneity can either be directly controlled or calculated in the theoretical flow problems – which paired with experimental results, is used to show that fluid retraction provides a direct measure of flow heterogeneity and viscoelastic aging. These findings highlight the capability of cessation of flow paired with rheo-PTV to quantify flow heterogeneity in a wide range of viscoelastic complex fluids, providing spatial information not accessed by other techniques.

2 Theory

2.1 Couette flow of two adjacent UCM fluids between parallel plates

A simple approximation of shear-banded flow of WLMs is Couette flow between parallel plates of two upper-convected Maxwell model (UCM) fluids, separated perpendicular to the flow direction (Fig. 1). For simplicity, these fluid regions A and B (Fig. 1) are each composed of only one species, which have distinct relaxation times and viscosities. The benefit of this flow problem is that the flow field can be solved analytically, which provides key insights into fluid retraction behavior during cessation of flow. Additionally, these analytical results demonstrate that rheo-PTV using this flow protocol can measure flow heterogeneity. Although this model is a fairly crude approximation of shear-banded flow, the key behaviors predicted by this model in cessation of flow protocols will be shown to match the trends observed in experiments.

The governing equations for Couette flow of two adjacent UCM fluids between parallel plates are:

$$\rho\frac{\partial \boldsymbol{v}}{\partial t} = -\rho\boldsymbol{v}\cdot\nabla\boldsymbol{v} - \nabla p + \nabla\cdot\boldsymbol{\sigma} \tag{1}$$

$$\tau_{\mathrm{i}}\overset{\nabla}{\boldsymbol{\sigma}} + \boldsymbol{\sigma} = \eta_{0,\mathrm{i}} 2\boldsymbol{D} \tag{2}$$

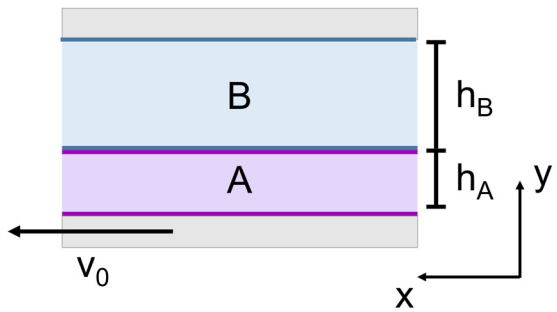

Fig. 1 Couette flow of two adjacent UCM fluids between parallel plates. The two fluid volumes are segregated perpendicular to the flow direction, with fluid A near the lower plate (y = 0) and fluid B near the upper plate ($y = h_A + h_B = H$).

Eqn (1) is the linear momentum balance, where $\boldsymbol{v}$ is the fluid velocity, ρ is the total mass density of the solution, p the pressure, and $\boldsymbol{\sigma}$ is the extra-stress tensor. Eqn (2) is the relationship of the extra-stress tensor for the UCM model, where τ_{i} is the relaxation time of fluid i = A, B, $\eta_{0,\mathrm{i}}$ is the zero-shear viscosity of fluid i = A, B, and $\boldsymbol{D} = \frac{1}{2}(\nabla\boldsymbol{v} + (\nabla\boldsymbol{v})^T)$ is the rate of strain tensor. The symbol $\overset{\nabla}{\boldsymbol{\sigma}}$ denotes the upper-convected derivative:

$$\overset{\nabla}{\boldsymbol{\sigma}} = \frac{\partial\boldsymbol{\sigma}}{\partial t} + \nabla\cdot(\boldsymbol{v}\sigma) - \boldsymbol{\sigma}\cdot\nabla\boldsymbol{v} - (\nabla\boldsymbol{v})^T\cdot\boldsymbol{\sigma} \tag{3}$$

The following criteria define the spatial extent of each fluid region within the gap:

$$0 \le y \le h_{\mathrm{A}} \quad \text{region A} \tag{4}$$

$$h_{\mathrm{A}} \le y \le h_{\mathrm{A}} + h_{\mathrm{B}} = H \quad \text{region B} \tag{5}$$

where h_{A} is the width of region A, h_{B} is the width of region B, and $H = h_{\mathrm{A}} + h_{\mathrm{B}}$ is the total gap width (Fig. 1). The governing equations of fluids A and B both apply at the interface between regions.

These governing equations are simplified considerably by assuming the flow is one-dimensional, $\boldsymbol{v} = (v_x,0,0)$, and inertial effects are negligible (creeping flow). These equations become:

$$\nabla\cdot\boldsymbol{\sigma} = 0 \tag{6}$$

$$\tau_{\mathrm{i}}\frac{\mathrm{d}\sigma_{yx}}{\mathrm{d}t} + \sigma_{yx} = \eta_{0,\mathrm{i}}\dot{\gamma} \tag{7}$$

$$\tau_{\mathrm{i}}\frac{\mathrm{d}\sigma_{xx}}{\mathrm{d}t} + \sigma_{xx} = 2\tau_{\mathrm{i}}\sigma_{xy}\dot{\gamma} \tag{8}$$

where $\dot{\gamma} = \frac{\mathrm{d}v_x}{\mathrm{d}y}$. Eqn (7) describes the evolution of the shear stress, σ_{yx}, and eqn (8) describes the evolution of the normal stress, σ_{xx}; eqn (8) is not needed to solve for the velocity. From eqn (6), the shear stress is constant across the gap of the flow geometry $\left(\frac{\mathrm{d}\sigma_{yx}}{\mathrm{d}y} = 0\right)$. Therefore the shear rates, $\dot{\gamma}_{\mathrm{A}}$ and $\dot{\gamma}_{\mathrm{B}}$, described by eqn (7) are constant within their respective regions:

$$\frac{\mathrm{d}}{\mathrm{d}y}\dot{\gamma} = \frac{\mathrm{d}}{\mathrm{d}y}\left(\frac{\tau_{\mathrm{i}}}{\eta_{0,\mathrm{i}}}\frac{\mathrm{d}\sigma_{yx}}{\mathrm{d}t} - \frac{1}{\eta_{0,\mathrm{i}}}\sigma_{yx}\right) = 0 \tag{9}$$

provided that $\eta_{0,\mathrm{i}}$ and τ_{i} do not change with y, which is true within each region A and B.

From eqn (7)–(9), a general solution for the evolution of the shear stress and shear rates in regions A and B is derived for a constant applied shear rate, $\dot{\gamma}_{\mathrm{app}}$ (see Section SI.1, ESI†). With no-slip boundary conditions assumed at each solid–fluid boundary, the resulting equations are:

$$\sigma_{yx}(t) = \eta_{0,\mathrm{eff}}\dot{\gamma}_{\mathrm{app}} + C\exp(-t/\tau_{\mathrm{eff}}) \tag{10}$$

$$\dot{\gamma}_{\mathrm{A}} = \frac{\dot{\sigma}_{yx}}{G_{0,\mathrm{A}}} + \frac{\sigma_{yx}}{\eta_{0,\mathrm{A}}} \tag{11}$$

$$\dot{\gamma}_{\mathrm{B}} = \frac{\dot{\sigma}_{yx}}{G_{0,\mathrm{B}}} + \frac{\sigma_{yx}}{\eta_{0,\mathrm{B}}} \tag{12}$$

where C is a constant that depends on the initial condition. The

shear stress evolution depends on the effective rheological properties across the gap. The effective zero-shear viscosity and elastic modulus are harmonic means of the properties in each fluid region weighted by the fraction the region occupies in the gap:

$$\frac{1}{\eta_{0,\mathrm{eff}}} = \frac{h_\mathrm{A}/H}{\eta_{0,\mathrm{A}}} + \frac{h_\mathrm{B}/H}{\eta_{0,\mathrm{B}}} \tag{13}$$

$$\frac{1}{G_{0,\mathrm{eff}}} = \frac{h_\mathrm{A}/H}{G_{0,\mathrm{A}}} + \frac{h_\mathrm{B}/H}{G_{0,\mathrm{B}}} \tag{14}$$

and $\tau_\mathrm{eff} = \eta_{0,\mathrm{eff}}/G_{0,\mathrm{eff}}$ is the effective relaxation time. This form of the effective viscosity has been proposed previously for perfectly lamellar multicomponent flows,[35,36] which are analogous to shear bands. In Section 4.4, eqn (10)–(12) are examined for cessation of flow. Analysis of the resulting equations is useful to build intuition about the relationship between flow heterogeneity and retraction. Results for shear startup flow are included in Section SI.1.1 (ESI†); however, these results do not provide insight into experiments, as the adjacent UCM model is an approximation of steady shear-banded flow and cannot make accurate predictions about the transient formation of flow heterogeneity. A more complex model is required to simulate the behaviors observed in both shear startup and cessation of flow experiments.

2.2 Couette flow of GCB model fluid between concentric cylinders

Analyzing Couette flow of adjacent UCM fluids between parallel plates reveals key insights about the nature of fluid retraction in heterogeneous flows. A second flow problem is explored using the GCB model, which allows spatiotemporal evolution of the microstructure and rheological properties and provides better qualitative agreement with experiments.[37] Briefly, the GCB model to describe WLMs simplifies the continuous distribution of WLM lengths into two discrete populations, A and B, where micelles in population A are double the length of species B. The viscoelasticity of both species is described by the UCM model, and the number densities of species A and B change dynamically in response to deformation.[20]

The flow geometry is two concentric cylinders – with a rotating inner cylinder of radius R_i and a stationary outer cylinder of radius R_o – which is the geometry used in most shear banding studies and the experiments performed here. An inherent radial stress gradient is present due to the curvature of the concentric cylinder geometry, which provides the initial source of heterogeneity to these flows. Couette flow of a GCB model fluid between concentric cylinders has been explored in-depth previously.[21,38] The description of the flow problem and solution procedure here are identical to that in prior work[39]; thus full details about governing equations, non-dimensionalization, and solution method are deferred to Section SI.2 (ESI†). Key details related to this flow problem are discussed below.

The evolution of the flow field and species populations for a GCB model fluid between concentric cylinders are examined in shear startup and cessation of flow protocols. The flow geometry is represented in cylindrical coordinates (r, θ, z) and the velocity is assumed to be one dimensional in the azimuthal direction, $\boldsymbol{v} = (0, v_\theta, 0)$. To simulate shear startup, the following boundary condition is imposed at the inner cylinder:

$$v_\theta(t, r = R_i) = v_0 \tanh(at) \tag{15}$$

and to simulate cessation of flow:

$$v_\theta(t, r = R_i) = v_0 \tanh(at) - v_0 \tanh(a(t - t_\mathrm{c})) \tag{16}$$

These boundary conditions simulate the finite time for a rheometer to change shear rates, where a is the ramp-rate and t_c is the onset of cessation of flow (time when the inner cylinder motion is stopped). The ramp-up rate of the rheometer is $a \sim O(1\text{–}10)$ ms. No-slip boundary conditions are assumed at both cylinder boundaries; therefore the applied shear rate is $\dot{\gamma}_0 = v_0/H$, where H is the gap width. Startup and cessation of flow are examined for one applied shear rate, which in dimensionless form is the Weissenberg number: $\mathrm{Wi} = \dot{\gamma}_0\tau_\mathrm{eff} = 5$, where τ_eff is the effective relaxation time of the GCB model. The dimensionless model parameters are fixed to values from ref. 39 (Table 1). Startup flow is stopped at several times t_c to examine the impact of the flow heterogeneity on fluid retraction as the stress relaxes.

3 Materials and methods

3.1 Materials

Wormlike micelles were formed from poloxamer P234 (Synperonic PE/P84, Sigma Aldrich) dissolved in HPLC-grade water (Fischer Scientific). Samples were stirred for ≥12 h at 4 °C until the poloxamer fully dissolved and were stored at 4 °C. Two formulations are examined: (1) 15% wt poloxamer in 2 M NaCl (Fischer Scientific) and (2) 4% wt poloxamer in 0.9 M NaF (Sigma Aldrich); materials were used as received. For brevity, (1) is referred to as P234-NaCl, and (2) as P234-NaF. Both formulations form entangled WLMs based on prior work (performed in D_2O),[14,34] and have properties in water similar to those in D_2O. Prior linear rheology measurements demonstrated that WLMs formed with NaF have faster relaxation dynamics than those formed with NaCl.[34,40] These measurements also suggested that P234-NaF WLMs are fast-breaking, but did not provide sufficient evidence to discern if P234-NaCl WLMs have longer contour lengths, slower breakage dynamics, or a combination of these effects. Different P234 concentrations are required to produce WLMs with greatly contrasting rheological behavior – hypothesized to result from differences in WLM contour length as these WLMs have approximately equal cross-sectional radii.[14,34] This work also builds upon previous nonlinear rheology characterization of 15% wt P234 WLMs.[14]

Table 1 Key dimensionless GCB model parameter values; see Section SI.2 (ESI) for more detail. Here, El is the elasticity number, β is the ratio of solvent viscosity to η_0, ε and μ are relaxation time ratios where $\varepsilon = \tau_\mathrm{B}/\tau_\mathrm{A}$ and $\mu = \tau_\mathrm{A}/\tau_\mathrm{eff}$, $\tilde{c}_\mathrm{Aeq}$ and $\tilde{c}_\mathrm{Beq}$ are dimensionless equilibrium breakage and recombination rates for species A and B, respectively, and $q = (R_o - R_i)/R_i$ is the curvature

Parameter	El^{-1}	β	ε	μ
Value	0	7×10^{-5}	1.2×10^{-3}	2
Parameter	$\tilde{c}_\mathrm{Aeq}$	$\tilde{c}_\mathrm{Beq}$	q	
Value	1	5	0.08	

3.2 Shear rheology

Linear viscoelastic (LVE) rheology and nonlinear controlled stress and shear rate tests were done on an Anton Paar MCR 302 stress-controlled rheometer. Measurements were performed with an evaporation blocker, at 43.5 °C for P234-NaF and 38.5 °C for P234-NaCl. Circulating fluid around the outer cylinder maintains the setpoint temperature. The geometry, also used for rheo-PTV, is a black anodized aluminum bob of radius R_i = 16.35 mm and length L = 16.5 mm moving in a transparent quartz cylinder of radius R_o = 17.5 mm (gap-to-radius ratio ε = 0.07; aspect ratio $\Gamma = L/(R_o - R_i)$ = 14.35).

The rheological properties of P234-NaCl and P234-NaF are very different, thus distinct rheology protocols were used. P234-NaCl rheology is very sensitive to the thermal treatment and sample age;[14] thus the pre-shear, thermal treatment, and rejuvenation protocols are almost identical to those in ref. 14. Flow curves were measured in P234-NaCl using both controlled stress (creep) and controlled shear rate protocols, where each data point was collected after 2–3 hours as done previously[14]; see Section SI.3 (ESI†) for complete rheology details. Note that due to aging effects, the shear stress may evolve even after these long measurement times, though not substantially.[14] Although viscoelastic aging was not observed in P234-NaF, a ten-minute equilibration period at T = 43.5 °C preceded all measurements, and the sample was rejuvenated between trials using the same protocol as for P234-NaCl (see Section SI.3, ESI†). The P234-NaF flow curve was measured to identify the likely shear banding region. As these WLMs did not have a yield stress, a single ramp-up shear rate protocol ($\dot{\gamma}$ = 0.02–10 s^{-1}) captured both the Newtonian region (low $\dot{\gamma}$) and the shear-banding plateau (intermediate $\dot{\gamma}$). The sample was sheared for ten minutes at each shear rate. The onset of the shear banding plateau agreed with the expected value for viscoelastic WLMs $\dot{\gamma}\tau \sim 1$,[41] where the relaxation time τ was calculated from the crossover of G' and G''.

3.3 Rheo-particle tracking velocimetry (rheo-PTV)

To visualize the flow field, simultaneous rheology and particle tracking velocimetry were performed using established instrumentation.[10,42] The same geometry used for LVE and flow curve data was used for rheo-PTV. A 0.3 mm laser light sheet (60–150 mW CNI 532 nm low noise) illuminates a small region of the quartz cell. Tracer particles added to the sample (200 ppm 8–12 μm TSI Hollow-glass spheres) scatter the incident light. Samples were sonicated for ≥5 min prior to loading to ensure particles were well-dispersed. Particle addition was confirmed not to significantly alter the rheology.

The shear protocol used in rheo-PTV measurements to probe the heterogeneity of the underlying fluid was a shear startup test followed by cessation of a flow, *i.e.* a period of time over which the strain is held constant. One shear rate in the shear banding region was characterized in-depth for each system: $\dot{\gamma}$ = 1 s^{-1} for P234-NaF and $\dot{\gamma}$ = 0.5 s^{-1} for P234-NaCl. The duration of startup prior to cessation of flow was chosen based on unique features in the stress response of long-shear startup trials.

During these protocols, particles within a region of interest were recorded using a Lucam Lm165 CCD camera. Particle positions were identified and tracked between images using the open-source Trackpy Python package,[43] which extends standard particle tracking algorithms.[44] The particle locations are converted from the image pixel coordinates to cylindrical coordinates, the natural coordinate system describing the particle trajectories.

3.4 Velocity profile calculation

Data points in the velocity profiles correspond to the motion of individual particles, where the velocity of each particle was calculated using a trajectory-fitting approach described in Section SI.4 (ESI†). Briefly, this approach estimates a particle's velocity by fitting a displacement function to all of the particle's positions over a time interval.[45] In typical rheo-PTV analysis, the velocity of a particle is calculated from its displacements between successive frame acquisitions.[18,46–48] The difference between these approaches is subtle, but the approach used in this work better estimates the velocity and associated uncertainty for transient flows with slow-moving or rapidly accelerating particles, both of which are observed in cessation of flow (*e.g.* Fig. S1, ESI†). These two analysis methods are described and compared in Section SI.4 (ESI†) and rigorously in ref. 45.

In shear startup, particle trajectories were fit assuming a constant particle velocity within short time intervals (~1–2 s), as done previously.[14] In cessation of flow, the velocity continuously decelerates and therefore the time interval must be adjusted dynamically. Velocities were first calculated using a slightly modified approach, by fitting full-duration trajectories with a decaying exponential-type function. This method was feasible because particles were present within the acquisition region throughout the duration of cessation of flow. For P234-NaF, a single exponential or sigmoid function was used; for P234-NaCl, a sum of two exponentials was used (see Section SI.4, ESI†). This approach provided time constants for the velocity decay and was compared with the averaging approach assuming constant velocity over short time intervals – where the time constants informed the time interval widths. Both approaches produced similar velocities (Fig. S4, ESI†).

For velocity profiles, the radial position in the gap is reported relative to the inner cylinder. The normalized gap position r/H = 0 at the inner cylinder and r/H = 1 at the outer cylinder. Uncertainty was estimated from the root-mean-square deviation of the predicted trajectory with velocity v_{avg} from the measured particle trajectory. Velocity profiles at equal startup times prior to flow cessation were reproducible for both formulations (Fig. S6 and S8, ESI†).

4 Results and discussion

4.1 Wormlike micelle characterization

While WLMs form in both 4% wt P234 in 0.9 M NaF and 15% wt P234 in 2 M NaCl, the rheological properties dramatically differ (Fig. 2). The linear and nonlinear rheology of P234-NaF

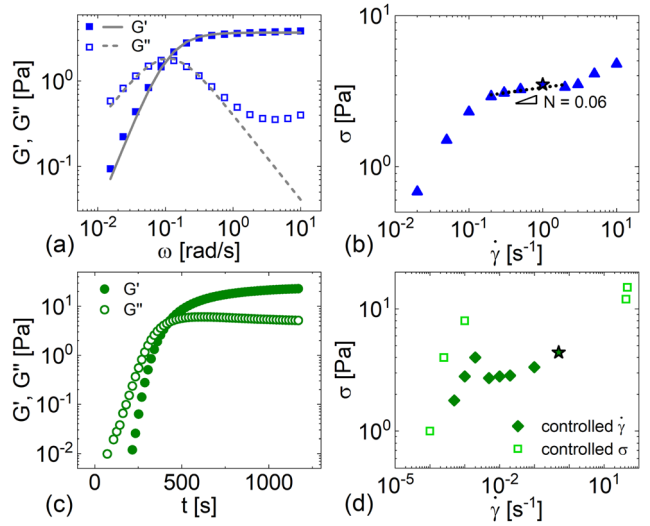

Fig. 2 Frequency sweep (a) and flow curve (b) of P234-NaF. (a) A Maxwell model fit (solid and dashed lines) yields estimates of $G_0 = 3.7 \pm 0.3$ Pa and $\tau = 9.1 \pm 0.4$ s. (b) Shear banding is expected in the flow curve plateau region ($\dot{\gamma} \approx 0.2$–$2\ s^{-1}$, $N = 0.06$). An SAOS aging test (c) and flow curve (d) of P234-NaCl. On each flow curve, ★ denotes the shear rate investigated in shear startup and cessation of flow.

resembles that expected for typical viscoelastic WLMs. The frequency sweep of P234-NaF (Fig. 2a) is well described by a single relaxation time Maxwell model in the low-to-moderate frequency region ($G_0 = 3.7 \pm 0.2$ Pa and $\tau = 9.1 \pm 0.6$ s). At higher frequencies, G'' deviates from this model, attributed to additional relaxation modes such as Rouse motion of the wormlike chains.[23,49] The flow curve of P234-NaF (Fig. 2b) has a Newtonian region at low shear rates, where the stress increases linearly with applied shear rate, followed by an apparent plateau region with a power law index $N = 0.06$ ($\dot{\gamma} \approx 0.2$–$2\ s^{-1}$), where shear banding is anticipated. The shear rate at the onset of this plateau agrees well with the expected value for typical viscoelastic WLMs ($\dot{\gamma}\tau \approx 2$).[8,41] The increase in shear stress at the end of the stress plateau likely corresponds to the onset of elastic instabilities, as seen in other WLM solutions.[47,50–52]

The gel-like rheological properties of P234-NaCl were previously characterized in D_2O,[14] but are characterized here due to differences in poloxamer batch and solvent. As a result, the viscoelastic aging rate is slightly faster in this formulation.[14] The storage modulus monitored with SAOS (Fig. 2c) requires 20 minutes at 38.5 °C to reach $G' = 24$ Pa – the benchmark storage modulus prior to startup. The flow curve of P234-NaCl here is similar to that previously reported.[34] In contrast to P234-NaF, here an apparent static yield stress is observed based on controlled-stress (creep) measurements (Fig. 2d). The nature of this apparent yield stress in P234-NaCl was discussed in-depth previously.[34] The static yield stress, $8 \leq \sigma \leq 12$ Pa, is slightly lower than in the prior formulation;[14] see Section SI.6 (ESI†) for full comparison.

The stark contrast in rheology between P234-NaF and P234-NaCl arises in part due to the different anion-specific interactions of fluoride anions compared to chloride anions,[53] which were previously shown to impact the zero-shear viscosity and relaxation time of 4% wt poloxamer WLMs.[34] Chloride anions promoted the formation of longer WLMs – with longer relaxation times – than fluoride anions. The increased poloxamer concentration in P234-NaCl compounds this effect, slowing the dynamics further and increasing the elastic modulus to roughly an order of magnitude greater than in P234-NaF. Most notably, these different formulations produce WLMs with distinct viscoelastic and gel-like properties, which have dramatically different transient behavior in shear startup.

4.2 Shear startup flows

Rheo-particle tracking velocimetry during shear startup confirms that both formulations exhibit heterogeneous flow or shear bands; however, the evolution of the velocity profiles is strikingly different (Fig. 3). These different routes to shear band formation are surprising if only the shear stress is considered; the evolution of the shear stress at applied shear rates $\dot{\gamma} = 1$ and $0.5\ s^{-1}$ for P234-NaF and P234-NaCl, respectively, have similar features (Fig. 3a and b). In both cases, the shear stress increases at a nearly linear rate during the initial elastic deformation of the solution. Then, at a strain $\gamma = \dot{\gamma}t \sim O(1)$, the stress reaches a maximum and subsequently decreases at a rapid rate. As time progresses, the shear stress decreases more slowly. A much longer time than shown in Fig. 3 is likely required to reach a steady state stress.[9]

For P234-NaF, shear bands form gradually during shear startup. The velocity profile is nearly linear throughout the stress overshoot of shear startup (Fig. 3c, $t = 4$ and 14 s). The velocity profile at the end of the stress overshoot only displays a slight degree of shear thinning (purple ▲, Fig. 3c, $t = 25$ s). As time progresses, the velocity profile gradually becomes more nonlinear, and eventually distinct shear bands form after a length of time much longer than the relaxation time (Fig. 3c, $t = 540\ s > 50\tau$). The evolution of the velocity profile for P234-NaF progresses similarly to that in typical viscoelastic WLM solutions like those formed from CPyCl-NaSal.[9,10] These shear startup results thus suggest that P234-NaF forms shear bands by the disentangle–re-entangle mechanism. Interestingly, for $r/H \leq 0.1$, the velocity profile is nearly linear and maintains the same slope at all times, indicating a local shear rate roughly equal to the gap-averaged shear rate. This peculiar, previously unreported behavior is discussed further in Section 4.7.

In contrast, the velocity profile becomes highly nonlinear early on in shear startup flow for P234-NaCl and eventually forms distinct fluidized and solid-like regions (Fig. 3d); this mechanism of shear band formation was analyzed in detail previously.[14] Briefly, shear bands form due to partial fluidization during the stress overshoot that becomes trapped due to viscoelastic aging, like in some soft glassy materials.[15,16] Unlike in P234-NaF, the velocity profile does not remain linear throughout the stress overshoot. Shear thinning in the velocity profile begins around the stress maximum (Fig. 3d, $t = 4$ s) and quickly develops into minor flow reversal as the stress rapidly decreases (Fig. 3d, $t = 17$ s). As time progresses, flow reversal subsides, and distinct regions form (Fig. 3d, $t = 150$ and 2150 s).

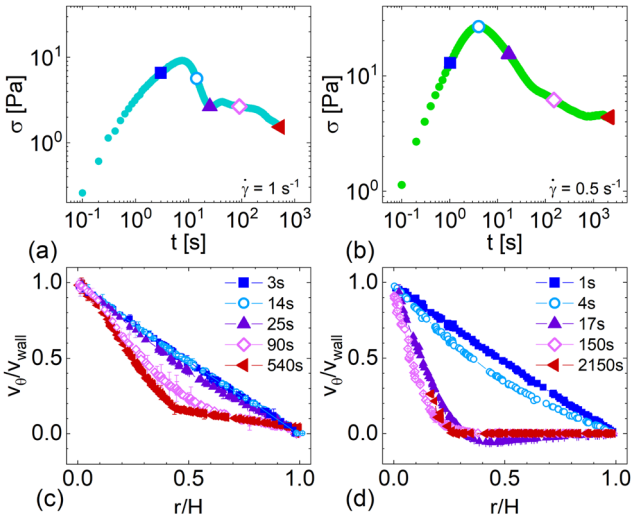

Fig. 3 Shear startups at $\dot{\gamma}$ = 1 s^{-1} for P234-NaF (a) and $\dot{\gamma}$ = 0.5 s^{-1} for P234-NaCl (b). The shear stress evolves with similar features for both WLMs, but the velocity profile evolution starkly differs. Velocity profiles of P234-NaF (c) gradually evolve toward distinct shear bands whereas velocity profiles of P234-NaCl (d) become dramatically nonlinear early in startup, with a period of flow reversal. At t = 2150 s, the velocity near the inner cylinder cannot be determined due to strong WLM alignment, leading to substantial scattering of the light reflected from the particles.[14]

4.3 Cessation of flow experiments

The flow kinematics of P234-NaF and P234-NaCl evolve very differently in shear startup, where the key difference is the presence of flow reversal prior to shear-banded flow in P234-NaCl. Two criteria were proposed for flow reversal during shear startup[14]: fluid elasticity and heterogeneity in the rheological properties during the region of decreasing shear stress in the overshoot. While both WLM formulations are elastic, the magnitude and spatial distribution of heterogeneity in the rheological properties during this time period are unclear. One issue in comparing the shear startup behavior is that the base flow counteracts – and can suppress – fluid retraction.[14] The cessation of flow experiments here remove this complication.

Here, startup flow is stopped during three key periods of shear startup: during the initial elastic deformation, during the rapid drop in stress, and after shear bands have fully formed. For P234-NaCl, substantial fluid retraction is anticipated to occur when the imposed flow is stopped during flow reversal. A smaller degree of retraction occurs in cessation of flow at the other two stop times. The magnitude of retraction upon flow cessation at each stop time reflects the expected degree of flow heterogeneity.

4.3.1 Cessation of flow: P234-NaF. Shear startup flow stopped at three times (t_c = 3, 14, 540 s; Fig. 4) reveals that fluid retraction occurs at each time, following: the initial elastic deformation, the rapid drop in shear stress after the stress maximum, and shear-banded flow. The shear stress is remarkably consistent across trials (Fig. 4a). As the shear stress relaxes (Fig. 4b–d), fluid retraction occurs (Fig. 4e–g), and the magnitude of the retraction speed decays as time progresses. The retraction speed is small when the flow is stopped in the stress overshoot (t_c = 3, 14 s in Fig. 4e and f): at maximum only 1–2% of the wall velocity during shear startup (v_{wall} = 1.1 mm s^{-1}). In comparison, the magnitude of the fluid retraction when shear-banded flow precedes cessation (Fig. 4g, t_c = 540 s) is an order of magnitude greater: at maximum ~15% of the wall velocity. Interestingly, the increased retraction speed occurs despite the fact that the shear stress here is approximately six times lower prior to flow cessation.

The majority of fluid retraction ceases ~7.5 s into cessation of flow (Fig. 4e–g), well before the shear stress has fully relaxed (Fig. 4b–d). The time constant for this velocity decay, τ_v, is shown for each trial in Table 2. This short time constant τ_v varies as expected for the disentangle–re-entangle mechanism in viscoelastic WLMs. This time constant is largest at the

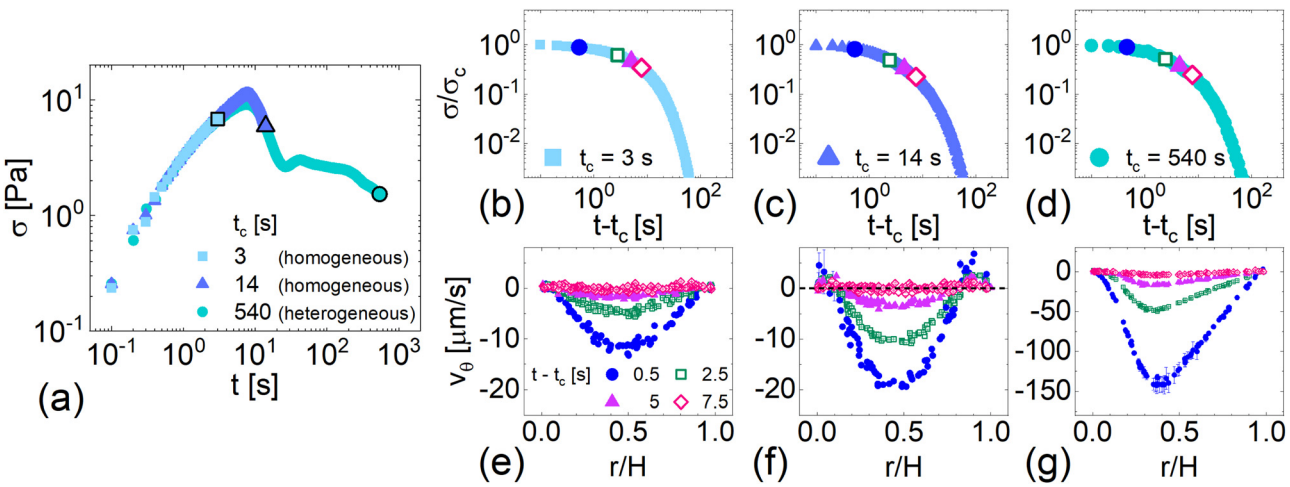

Fig. 4 Shear stress of P234-NaF in startup flow (a) at $\dot{\gamma}$ = 1 s^{-1} (v_{wall} = 1.1 mm s^{-1}) and in cessation of flow (b)–(d) after t_c = 3, 14, and 540 s. Outlined symbols in (a) indicate the stress before flow cessation, σ_c; the shear stress in (b)–(d) is normalized by σ_c. (e)–(g) Corresponding velocity profiles at four times during cessation of flow (indicated by legend in (e), same for each t_c). The magnitude of fluid retraction is greatest when shear banding precedes cessation of flow (g). The horizontal dotted line in (f) at v_θ = 0 is for visual aid. See Section SI.7.1 (ESI†) for individual velocity profiles.

Table 2 Cessation of flow time constants for P234-NaF

t_c [s]	3	14	540
τ_v [s]	2.1 ± 0.4	1.4 ± 0.2[a]	1.9 ± 0.1
$\tau_{s,1}$ [s]	1.8 ± 0.1	1.6 ± 0.1	1.6 ± 0.3
$\tau_{s,2}$ [s]	10.0 ± 0.1	9.5 ± 0.2	10.1 ± 1.2

[a] Indicates fit with sigmoidal function, see Section SI.4 (ESI). Each reported uncertainty is a 95% confidence interval around the fit value.

earliest time when WLMs are fully entangled (t_c = 3 s), drops in value when WLMs homogeneously disentangle (t_c = 14 s), and increases when a portion of fluid re-entangles (t_c = 540 s). Note this time constant also does not vary substantially with gap position (Fig. S5, ESI†).

Motivated by the presence of a fluid retraction timescale and prior work on CPyCl-NaSal surfactants during cessation of flow,[11] the shear stress was fit with a sum of two decaying exponentials (Section SI.8.1, ESI†) with time constants $\tau_{s,1}$ and $\tau_{s,2}$ (Table 2). The larger time constant is a similar value to the relaxation time of the WLM solution at rest (τ = 9.1 s). The smaller time constant agrees well with the time scale for fluid retraction. The physical significance of each time constant is discussed in Section 4.7.

Interestingly, when the flow is heterogeneous (shear-banded), the velocity profile is slightly asymmetric (Fig. 4g). The location of the maximum fluid velocity in retraction ($r/H \approx 0.39$) is close to the location of the shear band interface ($r/H \approx 0.43$). The location of the maximum retraction velocity also moves toward the inner wall as time progresses ($t - t_c$ = 0.5 *vs.* 2.5 in Fig. 4g).

4.3.2 Cessation of flow: P234-NaCl. The evolution of the shear stress and velocity profile in cessation of flow in P234-NaCl (Fig. 5) is starkly different than in P234-NaF, where flow was stopped at similar key periods during the stress evolution (t_c = 1.2, 17, and 2150 s; Fig. 5a). For P234-NaCl, fluid retraction is induced by stress relaxation at all stop times, but the relative magnitude of retraction trends differently with t_c than in P234-NaF. The shear stress decays almost an order of magnitude slower for P234-NaCl (Fig. 5b–d), but similar to P234-NaF, fluid retraction is fastest during a short interval after the start of the trial (Fig. 5e–g). Retraction is minimal when flow is stopped during the initial elastic deformation (t_c = 1.2 s, Fig. 5e); the maximum retraction velocity is ~1 μm s^{-1}, corresponding to a displacement of about one seed-particle diameter every 10 s. In contrast to P234-NaF, fluid retraction is largest when shear startup is stopped during the rapid drop in stress after the stress maximum (t_c = 17 s, Fig. 5f). The maximum fluid retraction speed is nearly 40% of the wall velocity during startup (v_{wall} = 0.56 mm s^{-1}). For cessation of flow following fully-developed shear-banded flow (t_c = 2150 s, Fig. 5g), the retraction speed is roughly an order of magnitude slower than at t_c = 17 s.

Beyond the large increase in fluid retraction speed after the shear stress maximum, the shape of the velocity profile also changes from symmetric to asymmetric (Fig. 5e *vs.* f, g). At t_c = 1.2 s, the velocity profile is roughly symmetric (Fig. 5e) like in P234-NaF. After the stress maximum, a region of fluid close to the inner cylinder fluidizes and creates heterogeneous flow. The width of the fluidized regions remains roughly constant after forming. The apex of the velocity profile soon after stopping the flow ($t - t_c$ = 0.5 s) is located at $r/H \approx 0.3$ for t_c = 17 s and $r/H \approx 0.2$ for t_c = 2150 s (Fig. 5f and g, respectively). These positions are close to the interface between the distinct fluid regions during startup flow, $r/H \approx 0.25$ (Fig. 3d). Note the band interface position fluctuates slightly in time during startup due to secondary flow in the fluidized region.[14] Although the width of the fluidized and unyielded regions does not change significantly, the distinction between these regions becomes more refined as time progresses. The apex of the velocity profile becomes sharper and the shear rate becomes

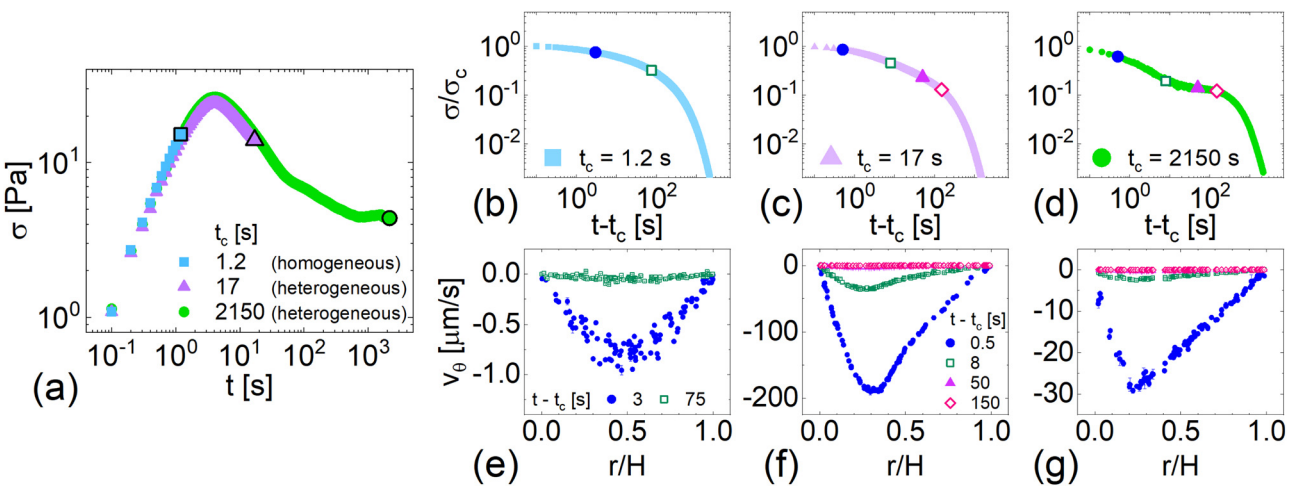

Fig. 5 Shear stress of P234-NaCl in startup flow (a) at $\dot{\gamma}$ = 0.5 s^{-1} (v_{wall} = 0.56 mm s^{-1}) and in subsequent cessation of flow (b)–(d) started after t_c = 1.2, 17, and 2150 s. Outlined symbols in (a) indicate σ_c; the shear stress in (b)–(d) is normalized by σ_c. Corresponding velocity profiles (e)–(g) are shown at four times during flow cessation; the same times are shown in (f) and (g). The fluid retraction magnitude is greatest during the rapid drop in stress after the stress maximum (f). See Section SI.7.2 (ESI†) for individual velocity profiles.

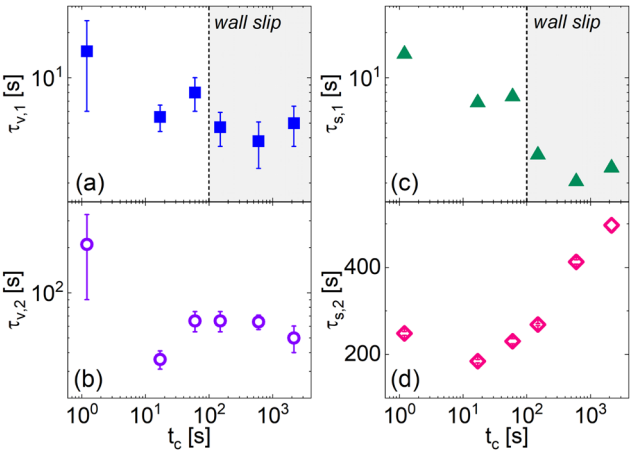

Fig. 6 Cessation of flow time constants for P234-NaCl. Time constants were extracted from fitting particle trajectories: (a) $\tau_{v,1}$ and (b) $\tau_{v,2}$ (Section SI.4, ESI†), and shear stress: (c) $\tau_{s,1}$ and (d) $\tau_{s,2}$ (Section SI.8.2, ESI†). Wall slip increases the speed of the fast fluid retraction (gray region in (a) and (c)) near the start of cessation of flow. The longest time constant, $\tau_{s,2}$, increases with t_c, indicating viscoelastic aging in the unyielded region.

almost constant within each region when the shear startup is performed for a longer time (Fig. 5f *vs.* g). Interestingly, retraction is accompanied by wall slip for t_c = 2150 s; in prior work,[14] wall slip in P234-NaCl also increased after flow reversal ceased.

Characteristic timescales for relaxation of the shear stress and retraction velocity change with t_c, revealing how the rheological properties of each region evolve during startup (Fig. 6). Fluid retraction and stress relaxation were measured for three more stop times (t_c = 60, 150, 600 s); see Fig. S22 in Section SI.9 (ESI†) for shear stress and velocity profiles. Four time constants are estimated during cessation of flow for each t_c: two from the decay of the velocity, $\tau_{v,1}$ and $\tau_{v,2}$, and two from the shear stress relaxation, $\tau_{s,1}$ and $\tau_{s,2}$. Time constants are obtained from fitting a sum of two decaying exponentials to the particle displacements (Section SI.4, ESI†) or shear stress (Section SI.8.2, ESI†). The time constants from particle displacements do not vary substantially with gap position (Fig. S5, ESI†).

All four time constants (Fig. 6a–d) decrease in value between the initial elastic deformation (t_c = 1.2 s) and the rapid stress decrease after the maximum (t_c = 17 s). Before the stress overshoot, the WLM solution is fully unyielded, and the structure and rheological properties across the flow geometry are mostly homogeneous. Notably, the time constants obtained from fitting the particle displacements and shear stress are similar.

After the stress overshoot, a large portion of the sample fluidizes. While the shorter time constants $\tau_{v,1}$ and $\tau_{s,1}$ remain similar (Fig. 6a and c), the longer time constants – which were similar before the overshoot (~200 s) – are an order of magnitude different after the overshoot (t_c = 17 s, $\tau_{v,2}$ = 36 s *vs.* $\tau_{s,2}$ = 184 s). The rapid drop in the time constant $\tau_{v,2}$ suggests this relaxation time is related to relaxation of the fluidized region, which will be much faster than for the unyielded region. In contrast, $\tau_{s,2}$ describes the relaxation of the unyielded region.

Assignments of these long relaxation times to particular fluid regions are verified by examining the evolution of these time constants as t_c increases. The evolution of the shorter time constants, $\tau_{v,1}$ and $\tau_{s,1}$, is similar and characterizes the quick fluid retraction at the onset of flow cessation (also observed in P234-NaF). These constants increase at t_c = 60 s and then decrease at larger t_c when wall slip becomes noticeable (Fig. 5g and Fig. S22e, f, ESI†). With wall slip, an effective shear rate is applied in the direction of retraction, which accelerates this process. The intermediate time constant, $\tau_{v,2}$, becomes roughly constant after flow reversal has ceased and distinct fluid regions have formed, $t_c \geq 60$ s; thus viscoelastic aging does not appear to impact this time constant. This observation and the magnitude suggest this time constant may depend primarily on the properties of the fluidized band.

Unlike the other time constants, $\tau_{s,2}$, the longest time constant, increases with t_c. The large value of $\tau_{s,2}$ suggests that this time constant depends on the relaxation time of the unyielded region. The rate of increase of $\tau_{s,2}$ slows as the shear startup progresses (Fig. 6d is a semi-logarithmic plot) – a characteristic feature of viscoelastic aging.[54] Therefore the evolution of $\tau_{s,2}$ strongly suggests that the unyielded region undergoes viscoelastic aging in shear startup; our prior work indicates that viscoelastic aging in this system is related to an increase in the micelle entanglement density, driven by an increase in the average contour length of the micelles.[14] Together, the evolution of the velocity profiles and this time constant provide strong evidence for the hypothesized shear-band formation mechanism of P234-NaCl.[14]

4.4 Fluid retraction of two adjacent UCM fluids between parallel plates

To explain the observed fluid retraction in cessation of flow, a simple flow problem is considered. Here, the fluid velocity evolution for two adjacent UCM fluids between parallel plates (Section 2.1) is examined upon flow cessation, where the applied shear rate is set to zero following flow startup.

4.4.1 Particular solution for cessation of flow. If the applied shear rate $\dot{\gamma}_{app}$ is set to zero after startup flow has elapsed for a time t_c, the stress will dissipate in time; however, flow will continue due to the heterogeneous properties of the fluid. To find a particular solution to eqn (10) for cessation of flow, the initial condition must be specified. For convenience, a time is defined since the onset of the cessation of flow protocol $t^* = t - t_c$. Therefore, the initial condition of the shear stress is $\sigma(t^* = 0) = \sigma_c(t_c)$ where $\sigma_c(t_c)$, the shear stress obtained in shear startup at a constant applied shear rate $\dot{\gamma}_{app} = \dot{\gamma}_0$ maintained for a time t_c, is given by:

$$\sigma_c(t_c) = \eta_{0,eff}\dot{\gamma}_0(1 - \exp(-t_c/\tau_{eff})) \quad (17)$$

Using this initial shear stress and changing the applied shear rate to zero, $\dot{\gamma}_{app} = 0$, the particular solution of eqn (10) for cessation of flow is:

$$\sigma_{yx}(t^*) = \sigma_c(t_c)\exp(-t^*/\tau_{eff}) \quad (18)$$

The shear stress relaxes exponentially like a homogeneous UCM fluid.

Despite the similarity in shear stress evolution, the flow field during cessation of flow with two adjacent UCM fluids is very different from that of a homogeneous UCM fluid. For a single UCM fluid, no fluid motion would be expected during this flow protocol. As the shear rate is constant in regions of fluid where the rheological parameters are equal (eqn (9)), here the shear rate would be constant through the gap and equal to the applied shear rate $\dot{\gamma}_{app} = 0$ imposed by the boundary conditions.

However, with two adjacent UCM fluids, the fluid retracts during the stress relaxation because the relaxation time of each fluid region is different, which is revealed by solving for the shear rates in both regions of fluid A and B. For parallel plate flow, the shear stress must be uniform across each region at all times, and therefore the time derivative of the shear stress is also uniform:

$$\frac{d\sigma_{yx,A}}{dt} = \frac{d\sigma_{yx,B}}{dt} \tag{19}$$

Rearranging the equations for the shear rates of fluid A and B (eqn (11) and (12)) and setting the derivatives of the shear stress equal yields:

$$G_{A,0}\dot{\gamma}_A - G_{B,0}\dot{\gamma}_B = \sigma_{yx}\left(\frac{1}{\tau_A} - \frac{1}{\tau_B}\right) \tag{20}$$

As a consequence of the no-slip condition at both boundaries and $\dot{\gamma}_{app} = 0$, the shear rates in either region must satisfy $\dot{\gamma}_B = -\dot{\gamma}_A h_A/h_B$ (found explicitly using the shear rate constraint of eqn (SI.1.3), ESI† and $v_w = 0$). Substituting this relation between shear rates and the particular solution for shear stress in eqn (18) into eqn (20) yields an equation for the evolution of $\dot{\gamma}_A$:

$$\dot{\gamma}_A = \left[\frac{h_B\sigma_c(t_c)}{h_B G_A + h_A G_B}\left(\frac{1}{\tau_B} - \frac{1}{\tau_A}\right)\right]\exp(-t^*/\tau_{eff}) \tag{21}$$

and similarly for $\dot{\gamma}_B$:

$$\dot{\gamma}_B = \left[\frac{h_A\sigma_c(t_c)}{h_B G_A + h_A G_B}\left(\frac{1}{\tau_A} - \frac{1}{\tau_B}\right)\right]\exp(-t^*/\tau_{eff}) \tag{22}$$

which describes retraction during cessation of flow.

The evolution of the shear stress and flow field in cessation of flow (eqn (18), (21) and (22)) is made clearer by the example in Fig. 7. Here, $\tau_B = 5\tau_A$, $h_B = 3h_A$, $G_{B,0} = 3G_{A,0}$. The stress is assumed to reach steady state before cessation of flow: $\sigma_c/G_{A,0} = \frac{\eta_{eff}}{\eta_A}\dot{\gamma}_0\tau_A$, where $\dot{\gamma}_0\tau_A = 5$ is the normalized applied shear rate. For this parameter set, the shear stress decays exponentially with a time constant $\tau_{eff}/\tau_A \approx 1.7$ (Fig. 7a). At the onset of flow cessation, significant fluid retraction occurs at a speed greater than the wall velocity of the preceding startup test, v_0 (Fig. 7b). As time progresses, the shear rate – and thus fluid velocity – decays exponentially with the same time constant, τ_{eff}, as the shear stress (Fig. 7a inset shows decay of $v_{min}(t)$, the minimum gap velocity).

4.4.2 Comparing key predictions with experiments. Key features of the fluid retraction in cessation of flow are revealed by analyzing eqn (21) and (22), which are qualitatively consistent with the experiments. First, the magnitude of retraction

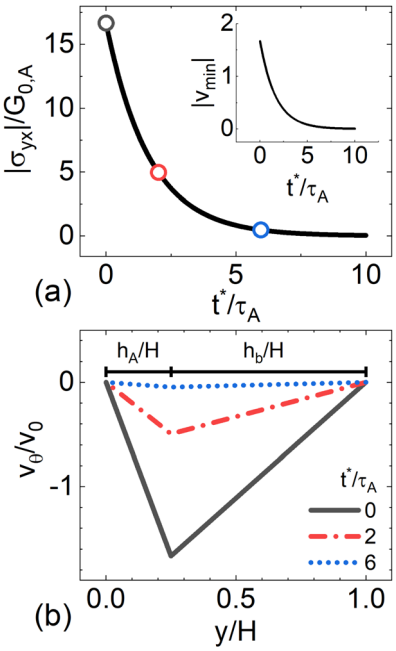

Fig. 7 Relaxation of normalized (a) shear stress and (b) velocity profiles at three times (○ in (a)) during flow cessation. Flow achieved steady state before flow was stopped; v_0 is the imposed wall velocity during the preceding shear. Time is normalized by the relaxation time of fluid A, τ_A; $t^* = t - t_c$ denotes the elapsed time after flow ceases. (a, inset) Shear stress and $|v_{min}|$ decay with the same time constant.

(magnitude of $\dot{\gamma}_A$, $\dot{\gamma}_B$) is large when the relaxation times in each region are dissimilar, which is expected in shear-banded flow. This feature is clearly seen for flow cessation in P234-NaF (Fig. 4e–g), where the retraction velocity at $t_c = 540$ s (flow is shear-banded and heterogeneous) is an order of magnitude greater than that at $t_c = 3$ and 14 s (homogeneous flow).

Second, the magnitude of retraction depends not only on the heterogeneity in rheological properties, but also on the shear stress magnitude before cessation of flow, σ_c. The magnitude of the shear rate (retraction velocity) scales with the shear stress in P234-NaCl; the retraction velocity is an order of magnitude higher at $t_c = 17$ s than at $t_c = 2150$ s primarily due to the much lower shear stress at the latter time (Fig. 5f and g). The dependence of retraction speed on shear stress also implies that the change in flow heterogeneity for P234-NaF at $t_c = 540$ s is understated, as σ_c at $t_c = 3$ and 14 s is $\sim 6\times$ greater than at $t_c = 540$ s.

Third, in the two adjacent UCM model fluids, the magnitude of both shear rates decays exponentially, with the same time constant as the shear stress, τ_{eff}. Unlike this model, the shear stress relaxes by multiple processes with different time constants in experiments. However, in both P234-NaF and P234-NaCl, the shortest relaxation time governing fluid retraction and shear stress are similar (Table 2 and Fig. 6), and, overall, the retraction velocity does decay with the shear stress as predicted.

Finally, the magnitude of the shear rates is inversely proportional to the elastic moduli of fluid A and B. The elastic modulus describes the stiffness in response to deformation, and thus fluids that have a higher elastic modulus are stiffer

and will deform less as the stress relaxes. This last observation is the reason that the maximum reaction speeds observed in P234-NaF (Fig. 4g) and P234-NaCl (Fig. 5f) are similar although the initial shear stress σ_c is over 10× higher in the latter case. The elastic modulus of P234-NaCl is an order of magnitude greater than P234-NaF, *i.e.* P234-NaCl WLMs are stiffer.

4.4.3 Basis for fluid retraction. To explain why fluid retraction occurs in the two adjacent UCM fluid model, the equality of the shear stress relaxation rate in eqn (19) is re-examined. The stress relaxation rates in fluids A and B are equal, and thus the following relation – obtained by rearranging eqn (11) and (12) and setting $\dot{\sigma}_{yx}$ equal – must be satisfied:

$$\frac{d\sigma_{yx}}{dt} = G_{A,0}\dot{\gamma}_A - \frac{1}{\tau_A}\sigma_{yx} = G_{B,0}\dot{\gamma}_B - \frac{1}{\tau_B}\sigma_{yx} \qquad (23)$$

The time derivative of the shear stress depends on two terms: one proportional to the shear rate, which is responsible for the buildup of stress during flow, and one proportional to the shear stress, which dissipates shear stress. The dissipation terms for A and B are not equal if the relaxation times are different. Thus to maintain a constant stress relaxation rate, fluid motion occurs. The fluid with the faster relaxation time experiences a shear rate in the same direction as the applied shear rate (continued deformation), which will slow the rate of stress relaxation. The fluid with the slower relaxation time experiences a shear rate opposite to the direction of the applied shear rate (strain recovery), which accelerates the rate of stress relaxation. For example, in Fig. 7b, the shear rate is negative in the faster relaxation time region, A ($r/H < 0.25$), which is the same sign as the applied shear rate during shear startup, $\dot{\gamma}_0$. Conversely, in Fig. 7b, the shear rate in the slower relaxation time region, B ($r/H > 0.25$), is positive (opposite sign of $\dot{\gamma}_0$). The balance of the terms in eqn (23) across both fluids produces an effective relaxation rate intermediate to both fluids.

While the GCB model and experimental systems have more complex dynamics than the flow problem with two adjacent UCM fluids, this principle holds true: substantial fluid deformation occurs during flow cessation when the fluid regions have much different relaxation times to offset large differences in the stress relaxation rate throughout the flow geometry.

4.5 Shear startup and fluid retraction of GCB model fluid between concentric cylinders

Whereas the first flow problem can be solved analytically, modeling the fluid behavior using the GCB model captures key flow phenomena in WLM gels in shear startup flows.[14] This startup behavior is outlined briefly below and elsewhere,[39] prior to focusing on behavior in cessation of flow.

4.5.1 Shear startup flow. The initially homogeneous radial distribution of species A and B in the GCB model evolves dramatically during shear startup, forming two regions with distinct populations of each species at steady state. At the onset of flow, the shear stress increases linearly with time (Fig. 8a), accompanied by a nearly linear velocity profile (Fig. 8b, t/τ_{eff} = 0.2) and nearly uniform number densities n_A and n_B across the gap (Fig. 8c and d, respectively, t/τ_{eff} = 0.2). As total mass is conserved, $2n_A + n_B$ is a constant. At the shear stress maximum (t/τ_{eff} = 0.45), the velocity profile becomes slightly nonlinear, a sizable fraction of species A breaks into species B, and the distribution of these populations becomes less uniform across the gap (Fig. 8c and d, t/τ_{eff} = 0.45).

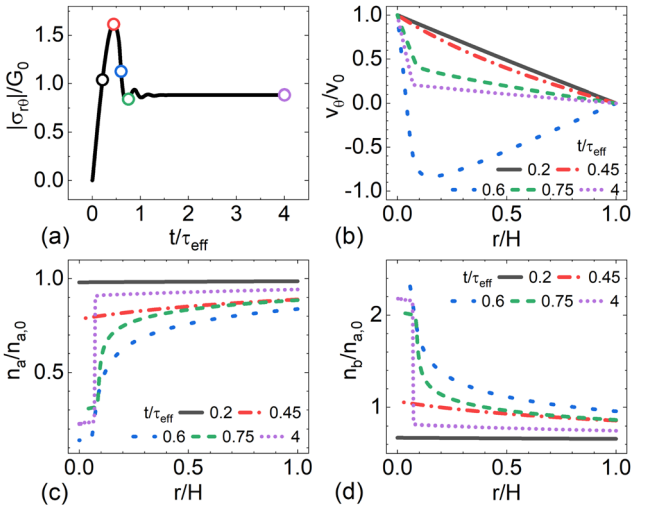

Fig. 8 Shear startup of GCB model WLMs at an applied shear rate of Wi = 5. (a) Shear stress evolution at the inner cylinder (r/H = 0). Normalized velocity (b), number density of species A (c), and number density of species B (d) are shown at five times during the shear stress evolution (○ in (a)). Shear stress is normalized by G_0, velocity by the imposed wall velocity v_0, and number densities of species A and B by the number density of species A at rest, $n_{A,0}$.

After the shear stress maximum, breakage of species A accelerates rapidly near the moving inner cylinder, and the populations n_A and n_B and flow field become highly nonuniform. At the halfway point in this stress drop (t/τ_{eff} = 0.6, blue ○ in Fig. 8a), substantial flow reversal develops, where the velocity is negative in a large portion of the gap (Fig. 8b). This flow reversal is accompanied by a highly nonuniform distribution of n_A and n_B across the gap, where n_A is significantly smaller near the inner wall (r/H = 0) than near the outer wall (r/H = 1), indicative of flow-induced breakage (Fig. 8c). Soon afterward, the shear stress reaches a local minimum at time t/τ_{eff} = 0.75, and two distinct regions of different shear rates and populations of species A and B become more refined (Fig. 8b–d). At this time flow reversal has ceased: the velocity is positive at all r/H. As time progresses, eventually the shear stress approaches a steady state. At t/τ_{eff} = 4, sharply defined shear bands are apparent in the velocity profile, and n_A and n_B also change almost discontinuously across the band interface, where species B is more prevalent in the high-shear-rate band and species A is more prevalent in the low-shear-rate band.

Comparing the evolution of the shear stress, velocity profile, and populations of species A and B during shear startup reveals that flow reversal coincides with highly heterogeneous fluid microstructure. Flow reversal during startup flow occurs for the same reason that fluid retraction occurs in cessation of flow in the two adjacent UCM fluid model. Shortly after the stress maximum, a large portion of species A rapidly breaks into species B, which has a much faster relaxation time $\tau_B = \varepsilon\tau_A \approx 10^{-3}\tau_A$.

This region rich in species B begins to rapidly dissipate the accumulated elastic shear stress, but the region rich in species A cannot dissipate stress at the same rate. Therefore, the region rich in A dissipates some of the elastic stress by retraction instead, like a rubber band retracts when tension is released. Here, the difference in the relaxation times of species A and B is so substantial that fluid retraction overcomes the base flow in shear startup.

4.5.2 Flow cessation to assess flow heterogeneity. Comparing retraction in cessation of flow after shear startups (Wi = 5) demonstrates that cessation of flow reflects the heterogeneity in the fluid microstructure and rheological properties across the flow geometry (Fig. 9). Here, flow was stopped at three times (t_c/τ_{eff} = 0.2, 0.6, 4) highlighted in Fig. 8, which also correspond with key regions of the shear startup where flow was stopped in experiments (initial ramp-up, rapid drop after stress maximum, and long-time response). Similar to observations from experiments, the magnitude of fluid retraction depends primarily on the degree of flow heterogeneity prior to flow cessation (*i.e.* the distribution of n_A and n_B across the gap, Fig. 8c and d).

During the initial ramp-up in shear startup (t_c/τ_{eff} = 0.2), the flow is nearly homogeneous (Fig. 8c and d, τ/τ_{eff} = 0.2, solid-black line), and minimal fluid retraction occurs as the stress decays upon cessation of flow (Fig. 9a and d). Although the fluid is essentially homogeneous here prior to flow cessation, slight shear thinning occurs due to the inherent stress gradient of the concentric cylinder geometry – leading to a small change in stress relaxation rate across the gap and minor fluid retraction. In practice, this fluid motion measured with standard velocimetry will quickly become virtually undetectable; recall v_{min} is the largest magnitude negative velocity in the gap at a given time, and for a gap width of 1 mm, $10^{-3}v_0 \sim 1\ \mu m\ s^{-1}$.

Conversely, upon cessation of flow after the stress maximum (t_c/τ_{eff} = 0.6, 4), the magnitude of fluid retraction is over two orders of magnitude larger than at t_c/τ_{eff} = 0.2 (Fig. 9d *vs.* e, f). The population distribution of species A and B at t_c/τ_{eff} = 0.2 is uniform, whereas the distribution of A and B at these later time points is highly heterogeneous (Fig. 8c and d, t_c/τ_{eff} = 0.6, 4, dashed-blue and dotted-green lines). The magnitude of fluid retraction also depends on the magnitude of the shear stress immediately preceding flow cessation, σ_c; at t_c/τ_{eff} = 0.6, σ_c and correspondingly the maximum magnitude of fluid retraction is over twice as large as those at t_c/τ_{eff} = 4 (t^*/τ_{eff} = 0.01 in Fig. 9b *vs.* c). While σ_c dictates the reversal magnitude for highly heterogeneous flows, the high degree of flow heterogeneity is a necessary precursor: the shear stress at t_c/τ_{eff} = 0.2 is greater than at t_c/τ_{eff} = 4, but the retraction magnitude is orders of magnitude larger in the latter case.

Notably, the retraction speed decelerates more quickly when the starting fluid is heterogeneous. For the two microstructurally-heterogeneous flows, fluid retraction has essentially ceased by t^*/τ_{eff} = 0.2 (Fig. 9e and f), whereas retraction is still ongoing at this time for the microstructurally-homogeneous flow (Fig. 9d). The heterogeneous flows contain a much greater proportion of species B everywhere in the gap, which relaxes stress much more quickly than species A and accelerates the effective relaxation rate of the fluid. Additionally, fluid retraction practically ceases well before the shear stress fully relaxes (Fig. 9a–c *vs.* d–f), which differs from the prediction of the two adjacent UCM fluid model. At long times, the retraction speed decays at a similar rate in all cases, with a time constant roughly equal to the effective relaxation rate τ_{eff} (Fig. S24, ESI†).

Heterogeneity of the fluid microstructure can be inferred not only from the magnitude of the velocity during retraction, but also from the shape of the velocity profile in cessation of

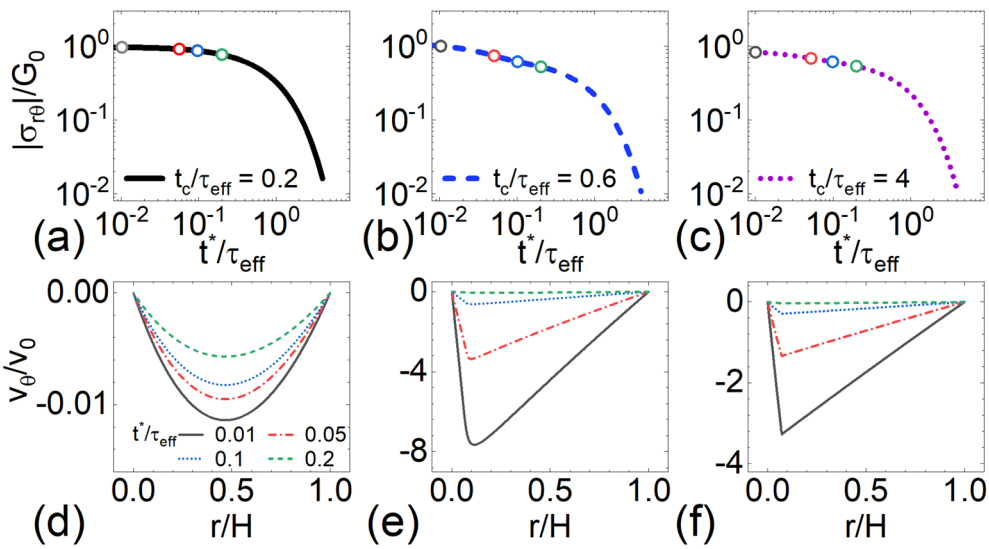

Fig. 9 Evolution of shear stress (a)–(c) and retraction velocity profiles (d)–(f) in cessation of flow following shear startup using the GCB model at Wi = 5, for three stop times: t_c/τ_{eff} = (a) and (d) 0.2, (b) and (e) 0.6, and (c) and (f) 4. Shear stress at the inner cylinder (r/H = 0) is normalized by the elastic modulus at rest, G_0. Velocity is normalized by the imposed wall velocity v_0; velocity profiles are shown at four times, t^*/τ_{eff}, during the stress relaxation following flow cessation (denoted by ○ in a–c).

flow (Fig. 9d–f). When cessation of flow begins before the stress maximum of the shear startup (t_c/τ_{eff} = 0.2), the velocity profile is nearly symmetric (Fig. 9d); in contrast, when cessation of flow begins after shear bands have fully formed (t_c/τ_{eff} = 4, Fig. 9f), two distinct regions of nearly constant shear rate are observed in the velocity profile. The intersection of these regions is also precisely the location of the shear band interface. Interestingly, for cessation of flow that commences during the rapid drop in stress in shear startup (t_c/τ_{eff} = 0.6, Fig. 9e), the velocity profile also has two regions of distinct shear rate, but the transition between these regions is not nearly as sharp as when shear-banded flow has fully formed prior to cessation.

The shapes of these velocity profiles correspond with the population distribution of species A and B during startup (Fig. 8c and d). When the population distribution changes gradually (t_c/τ_{eff} = 0.2, 0.45), the change in shear rate – the slope of the velocity profile – is also gradual. However, if the microstructure changes rapidly over a small spatial region (t_c/τ_{eff} = 0.6, 4), the shear rate also changes rapidly over that region. For shear-banded flow, the change in the fluid microstructure is essentially discontinuous, causing the discontinuity in shear rate in the velocity profile during cessation of flow.

4.5.3 GCB model predictions *vs.* experiments. GCB model predictions of the relationship between fluid heterogeneity and fluid retraction in cessation of flow are consistent with experiments. Notably, the shapes of the velocity profiles in the GCB model provided information about the degree of flow heterogeneity, which is consistent with the observations of these P234 WLM solutions. For P234-NaF, when homogeneous flow precedes cessation, t_c = 3 and 14 s, the velocity profile is approximately symmetric (Fig. 4e and f). Likewise, the GCB model predicts nearly symmetric velocity profiles when the flow is mostly homogeneous (Fig. 9d, t_c/τ_{eff} = 0.2). Slight shear thinning – and thus minor fluid retraction – occurs in experiments even when the flow is nearly homogeneous due to the inherent stress gradient of the flow geometry, which is also predicted by the GCB model.

Asymmetric velocity profiles indicate heterogeneous flow with the GCB model (Fig. 9e and f), where the apex of the velocity profile is located near the interface between the fluid regions during shear startup ($r/H \approx 0.1$, Fig. 8b). Similar behavior is observed when shear-banded flow fully develops in both P234-NaF and P234-NaCl (Fig. 4g and 5g, respectively). The evolution of the shape and magnitude of fluid retraction during cessation of flow in the GCB model and P234-NaCl are remarkably similar (Fig. 5 and 9). This similarity arises because heterogeneity becomes substantial in the flow geometry at a similar time during the stress evolution in both cases: right after the stress maximum. However, the maximum relative retraction velocity predicted by the GCB model when the flow is heterogeneous $v_\theta/v_0 \approx 3.8$ (Fig. 9e and f, respectively) is much greater than the maximum observed in P234-NaF ($v_\theta/v_0 \approx 0.1$) or P234-NaCl ($v_\theta/v_0 \approx 0.4$). One potential explanation for this difference could be that heterogeneity develops more quickly or to a greater magnitude in the GCB model than in experiments, which could lead to greater retraction. Further analysis of the growth of instabilities using the GCB model should be pursued as has been performed for other constitutive models.[24]

Finally, in both the GCB model predictions and experiments, the majority of fluid retraction occurs during only a portion of the shear stress relaxation. In the GCB model, retraction is tied to the rapid relaxation of stress carried by species B (Section SI.10, ESI†), which is the dominant species in the high-shear-rate band of fluid (Fig. 8d). The origin of these time constants is discussed in Section 4.7.

4.6 Limitations of the model predictions

Despite the success of these models in predicting many of the behaviors observed during cessation of flow, some phenomena that impact the evolution of the shear stress and velocity profiles were not captured. For example, in P234-NaF, a layer of fluid roughly 1/10th of the gap width is practically immobile at all times during cessation of flow for t_c = 3 and 540 s (Fig. 4e and g). Surprisingly, for t_c = 14 s (Fig. 4f), the fluid within this layer moves in the positive flow direction for a brief period (see Section SI.7.1, ESI†). Interestingly, the distinct region near the inner wall ($r/H < 0.1$) was also noticeable in shear startup (Fig. 3c), where the velocity in this region was roughly linear at all times. However, none of this behavior is captured by the models.

These results in shear startup and cessation suggest that the microstructure of P234-NaF changes near the boundary. Steady shear simulations that enforce a perpendicular orientation of the WLMs at the boundary[55] have predicted velocity profiles that are reminiscent of the shear-banded flow in Fig. 3c. In those prior simulations, the curvature of the flow geometry and strength of stress-induced diffusion influenced the spatial extent of these regions. Measurements in geometries with different gap widths could help resolve these effects.

Another phenomenon accompanying fluid retraction absent from the models considered here is wall slip. For P234-NaCl, wall slip became significant during fluid retraction (Fig. 5g) and accelerates the initial fast fluid retraction (Fig. 6a and b). Taking a closer look at the velocity profiles plotted individually (Section SI.7.2, ESI†), wall slip is still present even after this initial retraction. However, wall slip does not significantly impact the slower time constants (Fig. 6c and d) because at longer times macroscopic motion is minimal; the shear stress primarily relaxes due to internal dissipation. Nonetheless, the impact of wall slip on fluid retraction is important, and if more quantitative information is desired, the impact of wall slip needs to be considered.

4.7 Cessation of flow with rheo-PTV as a novel method for characterizing flow heterogeneity

The combination of experimental, theoretical and computational results demonstrates that cessation of flow characterized by rheo-PTV can provide a wealth of insights into flow heterogeneity in complex fluids. Substantial macroscopic, heterogeneous fluid motion in cessation of flow has been reported previously in polymer liquids[32]; however, this study is the first

to use this protocol to systematically study heterogeneous flow. Successful implementation of this protocol relies on newly developed analysis methods, where velocity is calculated from fits to particle trajectories rather than displacements between successive image acquisitions. The fluid velocity during cessation of flow often starts small and decays in time, and therefore the displacement between successive image acquisitions eventually becomes less than a fraction of the particle diameter. Velocity calculation from frame-to-frame displacements is impractical and will be plagued with noise. However, if particles are observed for long times, these displacements accumulate and become measurable. Therefore, even small velocities can be resolved when calculated by fitting the displacements. This method of velocity calculation is reminiscent of creep measurements used to characterize complex fluids: in creep, the shear rate is small, but because the cumulative strain is measured, even small shear rates can be discerned.

A significant advantage to this approach is that cessation of flow effectively detects heterogeneity in the rheological properties – information only partially accessible *via* microstructural techniques such as flow-SANS,[11,56] flow-SALS,[10,57] nuclear magnetic resonance spectroscopy (NMR),[58] and flow birefringence.[59,60] Each technique characterizes flow-induced microstructural anisotropy at specific length scales. However, connecting the microstructure to rheological properties is difficult; the length scales accessed by any individual technique only partially contribute to the WLM shear stress and rheological properties.[61,62]

Nevertheless, microstructural measurements can help interpret the velocity evolution in cessation of flow. The P234-NaF relaxation times are compared to the microstructural relaxation of CPyCl-NaSal WLMs in cessation of flow, measured with flow-SANS[11] and flow-SALS.[10] Similar to P234-NaF, the shear stress in cessation of flow of CPyCl-NaSal WLMs – which appear to shear band *via* a similar mechanism – relaxed with two distinct relaxation times. The slow relaxation time was three times longer than the fast one.[11] Interestingly, for P234-NaF the ratio of the relaxation times is similar ($\tau_{slow}/\tau_{fast} \approx 4$). The initial fast shear stress decay correlated with the decay of large density fluctuations, indicated by the disappearance of butterfly patterns in flow-SALS.[10] *Via* flow-SANS, WLM segmental alignment was shown to decay at the same rate as the slow relaxation stress decay.[11] In P234-NaF, the high-shear rate band is initially much brighter than the low-shear rate one, but this difference vanishes in $\sim$3 s, consistent with the observation that the shorter time constant corresponds to the relaxation of density fluctuations (Fig. S25 in Section SI.11, ESI†). The longer relaxation time of P234-NaF WLMs is thus presumed to decay with segmental alignment like in CPyCl-NaSal WLMs.

Linking the relaxation time constants in P234-NaCl to microstructural relaxation processes is more difficult. The shear banding mechanism is unique to these WLMs, and therefore no comparative microstructural studies exist. Unlike in P234-NaF, no visible brightness difference is apparent in the two fluid regions that can be attributed to density fluctuations. Additionally, three characteristic times describe the relaxation of shear stress and velocity in P234-NaCl instead of two like in P234-NaF. This extra relaxation time could be linked to the unique shear-banding mechanism of P234-NaCl. However, because the rheological properties of the fluid bands appear much more dissimilar in P234-NaCl than in P234-NaF, this timescale may just be better resolved for P234-NaCl. In P234-NaCl, the shortest relaxation time is two orders of magnitude faster than the longest, whereas the relaxation times are similar in P234-NaF. Complementary characterization is thus needed to resolve microstructural origins of these relaxation processes.

Although the timescales cannot be assigned to specific microstructural processes, the relatively large magnitude of these timescales in P234-NaCl may be related to the early development of flow heterogeneity. Prior work examining the origin of transient shear banding and fracture in polymer solutions found these phenomena can result from an elastic constitutive instability.[24,33] In step-strain or at early times in rapid shear startup, these solutions behave like an elastic solid, which is expected to be unstable for $0 < d\sigma/d\gamma$ – when a stress overshoot occurs.[63] The dynamics of P234-NaCl are sluggish enough that the initial deformation during shear startup at the shear rate examined here may be susceptible to a similar instability. The shear stress gradient inherent in the concentric cylinder geometry could provide the necessary inhomogeneity to amplify this elastic instability. Notably, in addition to strong flow heterogeneity after the stress maximum, prior work on P234-NaCl solutions found evidence of fracture when sample aging time was increased,[14] which is also connected to the proposed elastic instability. Investigation of shear-band formation at a range of shear rates in these WLM solutions and in others with a wider range of rheological properties will be useful to understand the transition between the shear-banding behaviors observed P234-NaCl and P234-NaF.

5 Conclusion

This work showcases a novel rheology protocol combining cessation of flow with rheo-particle tracking velocimetry (PTV), which reveals new information about heterogeneous shear flows that can occur in wormlike micelle (WLM) solutions. Paired with new PTV analysis methods used to accurately calculate velocities of slowing particles, this approach then enables fluid retraction upon flow cessation to be precisely detected and quantified for the first time. While many WLM solutions develop flow heterogeneity, only a handful of experiments have observed flow reversal – when a portion of the fluid moves opposite to the direction of the moving boundary – despite predictions by constitutive models.

To address this apparent discrepancy, this work aimed to experimentally and theoretically confirm two criteria previously proposed to be necessary to observe flow reversal based on evidence across wide-ranging soft materials. These criteria suggested that regardless of fluid composition, to observe flow reversal in shear startup: (1) the system must have elasticity; (2) flow must already be highly heterogeneous while the stress decreases in the stress overshoot region. To confirm these criteria, the base flow was removed and fluid retraction was

directly measured upon flow cessation in two poloxamer WLMs – a viscoelastic, fluid-like WLM (P234-NaF) and a gel-like WLM (P234-NaCl).

Canonical WLMs (P234-NaF) were hypothesized to exhibit minimal retraction when flow was stopped in the decreasing region of the stress overshoot, whereas gel-like WLMs (P234-NaCl) were expected to significantly retract in this region due to earlier-onset heterogeneity formation. Subsequent experiments confirmed these hypotheses and were in qualitative agreement with results from two theoretical Couette flow problems: (1) two adjacent Upper Convected Maxwell (UCM) model fluids between parallel plates, and (2) a Germann–Cook–Beris model fluid between concentric cylinders.

The minimal retraction exhibited by P234-NaF following flow cessation in the stress overshoot region is consistent with the ''disentangle–re-entangle'' mechanism widely accepted for canonical WLMs. As heterogeneous flow forms far beyond the stress overshoot region *via* this mechanism, significant fluid retraction upon flow cessation occurs in P234-NaF only when flow is stopped after shear bands have stabilized. In contrast, heterogeneous flow forms near the stress maximum in P234-NaCl, leading to substantial retraction upon cessation of flow. Particle trajectories were then analyzed to extract time- and spatially-dependent relaxation behavior, confirming the prior hypothesis that the low shear rate band in this WLM gel becomes trapped by viscoelastic aging.

This work thus reveals that flow reversal upon shear startup is not observed in P234-NaF (or any previously-reported canonical, fast-breaking WLMs) despite model predictions due to the difference in when the heterogeneity manifests: models predict that these flows become heterogeneous in the stress overshoot region, whereas in experiments, heterogeneity onsets at far longer times. Strikingly, theoretical predictions from these simplified models regarding the magnitude, shape, and lifetime of the retraction velocity profile are highly consistent with experiments on gel-like WLMs, in part due to the similarity in the onset of flow heterogeneity. Conversely, canonical WLMs exhibit nearly homogeneous flow in the stress overshoot region, leading to minimal fluid retraction; thus flow reversal is not observed because the minimal fluid retraction cannot overcome the imposed flow. Notably, we also show that cessation of flow combined with PTV can be used to extract quantitative, spatially-dependent information about heterogeneous flows whether or not flow reversal occurs, making this technique applicable for characterizing wide-ranging complex fluids. Importantly, because the method proposed here analyzes displacements, even small retraction velocities can be observed when heterogeneity is minimal.

While this approach can be used to extract time- and spatially-dependent rheological behavior in wide-ranging soft materials, more work remains to extract more quantitative information about the rheological properties of the heterogeneous flow regions. For example, once shear bands have formed, the viscosity in each band can be estimated from the shear rate. Based on the analytical solution for the two adjacent UCM fluids, the elastic modulus and relaxation times in each fluid region may be able to be extracted by performing retraction experiments at additional shear rates. Quantifying the shear rate and total accumulated strain will also be useful to compare experiments to models and estimate these parameters.

A final outstanding question is to determine which properties dictate the shear band formation mechanism. Experimentally, complementary microstructural characterization *via* techniques like flow-small angle light and neutron scattering will be essential to achieve this goal. Additionally, further analysis of WLM models will be crucial for identifying key parameters that influence the amplification of flow heterogeneity. Perhaps a more sophisticated model than those used here can describe both shear-band formation mechanisms showcased in this work.

Conflicts of interest

There are no conflicts to declare.

Acknowledgements

This work was supported by the National Science Foundation Graduate Research Fellowship (Award 2237827). The authors thank the Anton Paar VIP program for the rheometer used in this work.

Notes and references

1 T. Divoux, M. A. Fardin, S. Manneville and S. Lerouge, *Annu. Rev. Fluid Mech.*, 2016, **48**, 81–103.
2 S. Lerouge and J.-F. Berret, *Polymer Characterization*, Springer, 2009, pp. 1–71.
3 D. Bonn, M. M. Denn, L. Berthier, T. Divoux and S. Manneville, *Rev. Mod. Phys.*, 2017, **89**, 035005.
4 P. D. Olmsted, *Rheol. Acta*, 2008, **47**, 283–300.
5 S. M. Fielding, *Soft Matter*, 2007, **3**, 1262–1279.
6 S. M. Fielding, *J. Rheol.*, 2016, **60**, 819–820.
7 S. Manneville, *Rheol. Acta*, 2008, **47**, 301–318.
8 J.-F. Berret, *Langmuir*, 1997, **13**, 2227–2234.
9 O. Radulescu, P. Olmsted, J. Decruppe, S. Lerouge, J.-F. Berret and G. Porte, *Europhys. Lett.*, 2003, **62**, 230.
10 Y. T. Hu and A. Lips, *J. Rheol.*, 2005, **49**, 1001–1027.
11 C. R. López-Barrón, A. K. Gurnon, A. P. Eberle, L. Porcar and N. J. Wagner, *Phys. Rev. E: Stat., Nonlinear, Soft Matter Phys.*, 2014, **89**, 042301.
12 H. Mohammadigoushki, A. Dalili, L. Zhou and P. Cook, *Soft Matter*, 2019, **15**, 5483–5494.
13 S. R. Raghavan and Y. Feng, *Wormlike Micelles*, Royal Society of Chemistry, 2017, pp. 9–30.
14 P. J. McCauley, C. Huang, L. Porcar, S. Kumar and M. A. Calabrese, *J. Rheol.*, 2023, **67**, 661–681.
15 J. D. Martin and Y. T. Hu, *Soft Matter*, 2012, **8**, 6940–6949.
16 A. Kurokawa, V. Vidal, K. Kurita, T. Divoux and S. Manneville, *Soft Matter*, 2015, **11**, 9026–9037.

17 T. Divoux, D. Tamarii, C. Barentin and S. Manneville, *Phys. Rev. Lett.*, 2010, **104**, 208301.
18 P. Rassolov and H. Mohammadigoushki, *J. Rheol.*, 2020, **64**, 1161–1177.
19 J. Adams and P. D. Olmsted, *Phys. Rev. Lett.*, 2009, **102**, 067801.
20 N. Germann, L. Cook and A. N. Beris, *J. Non-Newtonian Fluid Mech.*, 2013, **196**, 51–57.
21 N. Germann, L. Cook and A. Beris, *J. Non-Newtonian Fluid Mech.*, 2014, **207**, 21–31.
22 L. Zhou, P. A. Vasquez, L. P. Cook and G. H. McKinley, *J. Rheol.*, 2008, **52**, 591–623.
23 L. Zhou, G. H. McKinley and L. P. Cook, *J. Non-Newtonian Fluid Mech.*, 2014, **211**, 70–83.
24 J. Adams, S. M. Fielding and P. D. Olmsted, *J. Rheol.*, 2011, **55**, 1007–1032.
25 E. Miller and J. P. Rothstein, *J. Non-Newtonian Fluid Mech.*, 2007, **143**, 22–37.
26 P. Rassolov and H. Mohammadigoushki, *J. Rheol.*, 2023, **67**, 169–181.
27 T. Divoux, C. Barentin and S. Manneville, *Soft Matter*, 2011, **7**, 9335–9349.
28 K. A. Erk, J. D. Martin, Y. T. Hu and K. R. Shull, *Langmuir*, 2012, **28**, 4472–4478.
29 S. Ravindranath, S.-Q. Wang, M. Olechnowicz and R. P. Quirk, *Macromolecules*, 2008, **41**, 2663–2670.
30 R. Benzi, T. Divoux, C. Barentin, S. Manneville, M. Sbragaglia and F. Toschi, *Phys. Rev. Lett.*, 2021, **127**, 148003.
31 R. B. Bird, R. C. Armstrong and O. Hassager, *Dynamics of polymeric liquids. Vol. 1: Fluid mechanics*, John Wiley and Sons Inc., New York, NY, 1987, pp. 78–79.
32 S.-Q. Wang, S. Ravindranath, P. Boukany, M. Olechnowicz, R. P. Quirk, A. Halasa and J. Mays, *Phys. Rev. Lett.*, 2006, **97**, 187801.
33 O. S. Agimelen and P. D. Olmsted, *Phys. Rev. Lett.*, 2013, **110**, 204503.
34 P. J. McCauley, S. Kumar and M. A. Calabrese, *Langmuir*, 2021, **37**, 11676–11687.
35 M. Gvaramia, G. Mangiapia, V. Pipich, M.-S. Appavou, S. Jaksch, O. Holderer, M. D. Rukhadze and H. Frielinghaus, *Colloid Polym. Sci.*, 2019, **297**, 1507–1517.
36 M. Awad and Y. Muzychka, *Exp. Therm. Fluid Sci.*, 2008, **33**, 106–113.
37 N. Germann, L. Cook and A. Beris, *J. Non-Newtonian Fluid Mech.*, 2016, **232**, 43–54.
38 N. Germann, A. Kate Gurnon, L. Zhou, L. Pamela Cook, A. N. Beris and N. J. Wagner, *J. Rheol.*, 2016, **60**, 983–999.
39 P. J. McCauley, M. A. Calabrese and S. Kumar, *J. Non-Newtonian Fluid Mech.*, 2023, **1**, 1–2.
40 D. Y. Zhang and M. A. Calabrese, *Soft Matter*, 2022, **18**, 3993–4008.
41 N. Spenley, M. Cates and T. McLeish, *Phys. Rev. Lett.*, 1993, **71**, 939.
42 Y. T. Hu, C. Palla and A. Lips, *J. Rheol.*, 2008, **52**, 379–400.
43 D. B. Allan, T. Caswell, N. C. Keim, C. M. van der Wel and R. W. Verweij, *soft-matter/trackpy: Trackpy v0.5.0*, 2021.
44 J. C. Crocker and D. G. Grier, *J. Colloid Interface Sci.*, 1996, **179**, 298–310.
45 P. J. McCauley, PhD thesis, Understanding self-assembly and flow heterogeneities in poloxamer wormlike micelles, University of Minnesota, 2023, pp. 57–75.
46 S. Manneville, A. Colin, G. Waton and F. Schosseler, *Phys. Rev. E: Stat., Nonlinear, Soft Matter Phys.*, 2007, **75**, 061502.
47 M.-A. Fardin, T. Divoux, M. Guedeau-Boudeville, I. Buchet-Maulien, J. Browaeys, G. H. McKinley, S. Manneville and S. Lerouge, *Soft Matter*, 2012, **8**, 2535–2553.
48 P. Cheng, M. C. Burroughs, L. G. Leal and M. E. Helgeson, *Rheol. Acta*, 2017, **56**, 1007–1032.
49 R. Granek and M. Cates, *J. Chem. Phys.*, 1992, **96**, 4758–4767.
50 S. Lerouge, M.-A. Fardin, M. Argentina, G. Grégoire and O. Cardoso, *Soft Matter*, 2008, **4**, 1808–1819.
51 M.-A. Fardin, B. Lasne, O. Cardoso, G. Grégoire, M. Argentina, J.-P. Decruppe and S. Lerouge, *Phys. Rev. Lett.*, 2009, **103**, 028302.
52 A. Briole, L. Casanellas, M.-A. Fardin, C. Py, O. Cardoso, J. Browaeys and S. Lerouge, *J. Rheol.*, 2021, **65**, 1187–1200.
53 B. A. Deyerle and Y. Zhang, *Langmuir*, 2011, **27**, 9203–9210.
54 Y. M. Joshi and G. Petekidis, *Rheol. Acta*, 2018, **57**, 521–549.
55 J. Adams, S. Fielding and P. Olmsted, *J. Non-Newtonian Fluid Mech.*, 2008, **151**, 101–118.
56 M. A. Calabrese, S. A. Rogers, L. Porcar and N. J. Wagner, *J. Rheol.*, 2016, **60**, 1001–1017.
57 J. Decruppe, S. Lerouge and J. Berret, *Phys. Rev. E: Stat., Nonlinear, Soft Matter Phys.*, 2001, **63**, 022501.
58 E. Fischer and P. T. Callaghan, *Phys. Rev. E: Stat., Nonlinear, Soft Matter Phys.*, 2001, **64**, 011501.
59 J. Decruppe, R. Cressely, R. Makhloufi and E. Cappelaere, *Colloid Polym. Sci.*, 1995, **273**, 346–351.
60 S. Lerouge, J.-P. Decruppe and P. Olmsted, *Langmuir*, 2004, **20**, 11355–11365.
61 E. Helfand and G. H. Fredrickson, *Phys. Rev. Lett.*, 1989, **62**, 2468.
62 M. E. Helgeson, P. A. Vasquez, E. W. Kaler and N. J. Wagner, *J. Rheol.*, 2009, **53**, 727–756.
63 G. Marrucci and N. Grizzuti, *J. Rheol.*, 1983, **27**, 433–450.

